



Microwave frequency transfer over 3000-km fiber based on optical frequency combs and active noise cancellation

Dongrui Yu ¹, Ziyang Chen ^{1,*}, Yufei Zhang ¹, Ziyi Jin ², Song Yu,² Bin Luo ² and Hong Guo ^{1,†}

¹State Key Laboratory of Advanced Optical Communication Systems and Networks, School of Electronics, and Center for Quantum Information Technology, Peking University, Beijing 100871, China

²State Key Laboratory of Information Photonics and Optical Communications, Beijing University of Posts and Telecommunications, Beijing 100876, China



(Received 21 December 2023; accepted 28 February 2024; published 1 April 2024)

Time and frequency transfer plays an important role in the fields of navigation and positioning, remote sensing, and fundamental physics. The performance of long-haul frequency transfer is ultimately limited by accumulated phase and amplitude noise in fiber propagation. In this work we overcome these limitations and demonstrate a frequency transfer system over 3000 km of indoor spooled fibers via repetition-frequency-locked frequency combs, which benefit from the extremely high signal-to-noise ratio. With the help of the digital phase discrimination and compensation method and active power stabilization, the dramatic phase and amplitude variations are sufficiently suppressed, respectively, which results in the residual instability 7.5×10^{-14} at 1 s and 1.0×10^{-16} at 10 000 s, without optical-electrical-optical recovery by the regeneration system. Our results mark a breakthrough in building large-scale, high-precision synchronization networks.

DOI: [10.1103/PhysRevResearch.6.023005](https://doi.org/10.1103/PhysRevResearch.6.023005)

I. INTRODUCTION

Transferring the state-of-the-art atomic clocks' frequency instability via optical means (i.e., optical time and frequency transfer, O-TFT) provides a pathway and infrastructure for numerous fields, including the redefinition of the fundamental unit of the “second” [1–3], navigation and positioning [4,5], remote sensing [6,7], and fundamental physics, such as atomic clock comparison [8–10], fundamental constants measurements [11,12], and dark matter detection [13,14].

There are two methods to realize O-TFT. One is based on the phase of the continuous-wave optical carriers, and the other one is based on the phase of the radio-frequency signal loaded on the optical carriers. The former approach has achieved a significant milestone with a high-performance remote transfer spanning 1840 km, demonstrating stability levels of 2×10^{-15} at 1 s and 4×10^{-19} at 100 s [15,16]. The latter method, which achieves the 10^{-16} order stability after a long averaging time, is capable of transferring most of the microwave clock signals [17–21]. The O-TFT can be implemented both in the free space and in the commercial fiber. The free-space scheme has made dramatic progress in hundred-kilometer-order transfer in past decades [22–27], while the O-TFT via installed optical fibers, benefiting from the shielded environment, has great potential to achieve uninterrupted long-haul transmission [28,29].

Particularly, for the radio-frequency O-TFT, introducing long-distance fibers inevitably brings multiple technical challenges. First of all, compared with short links, the link attenuation resulting from several thousand kilometers of fiber exceeds hundreds of decibels, and using multiple electrical repeaters to realize optical-electrical-optical conversion and recover the signal's energy remarkably increases the link noise. Moreover, temperature-induced phase drift in long fibers, proportional to the fiber length, easily exceeds the range of the phase discriminator and the analog phase shifter, resulting in fast losing lock. In order to preserve the signal-to-noise ratio (SNR) and ensure the instability in long-distance frequency transmission, it is generally necessary to use an electrical repeater to recover the reduced SNR [30–32]. Nevertheless, increasing the construction of an electrical repeater will not only increase the potential noise sources of the whole system but also greatly complicate the infrastructure. As a countermeasure, it is essential to develop an optical-frequency-comb-based (OFC-based) non-electrical-repeater radio-frequency transmission, because of their high SNR and the potential to maintain for longer distance in the fiber link [19–21,33–35].

In this work we extend the non-electrical-repeater OFC-based link using two carrier-envelope-offset (CEO)-free combs to 3000 km of fiber by overcoming severe phase and amplitude fluctuations induced by the ultralong fiber link. A series of technical breakthroughs have reduced the instability of the system dramatically. Firstly, in the fiber link we develop the low-noise erbium-doped fiber amplifiers (EDFAs) with the noise figure (NF) below 4.0 (typically 3.8), which is closer to the EDFA 3-dB noise limit in comparison with commercial devices. The channel attenuation beyond 600 dB induced by the 3000-km link is well compensated by the cascaded EDFAs. Secondly, we suppress the relative intensity noise

*chenziyang@pku.edu.cn

†hongguo@pku.edu.cn

Published by the American Physical Society under the terms of the [Creative Commons Attribution 4.0 International](https://creativecommons.org/licenses/by/4.0/) license. Further distribution of this work must maintain attribution to the author(s) and the published article's title, journal citation, and DOI.

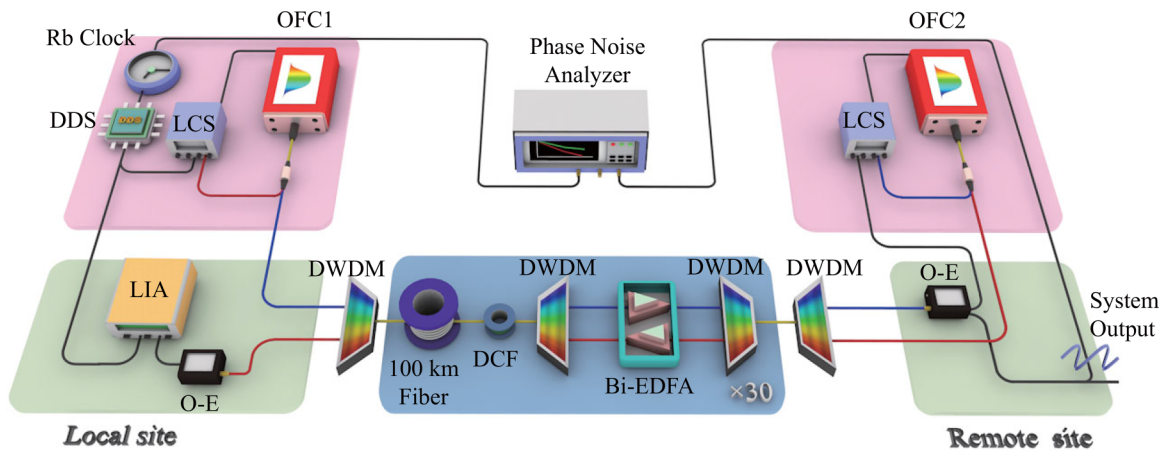


FIG. 1. Experimental setup. The Rb clock's signal is multiplied to 100 MHz, fed into the direct digital frequency synthesizer (DDS, for phase conjunction compensation), and loaded to the local OFC's repetition frequency with the locking control system (LCS). The local OFC signal serves as the carrier and is transferred to the remote site through the laboratory 3000-km link C32 channel of dense-wavelength division multiplexer (DWDM). The attenuation and dispersion are compensated by bidirectional erbium-doped fiber amplifiers (bi-EDFA) and dispersion compensation fiber (DCF). At the remote site, the arrived optical signal power is actively stabilized and converted to an electrical signal with the optical-electrical conversion system (O-E), and its first harmonic serves as the system output and the reference of the remote OFC. The remote OFC signal carrying the link's phase information is transferred to the local site through the C34 channel. The fiber-induced phase fluctuation is measured by the lock-in amplifier (LIA) at the local site and compensated by the DDS.

(RIN) with active power stabilization. This step is necessary since the ultralong fiber link induces serious power variation, which brings phase fluctuation through amplitude-to-phase conversion (APC). Thirdly, by using the high-precision digital phase discrimination and compensation technology, the significant phase drift exceeding tens of signal periods, which is an inevitable result when the link length reaches the thousand-kilometer order, can be sufficiently canceled. Other techniques are also exploited to ensure the system's robustness, such as the cavity-length temperature feedback control [36]. We show that two frequency signals at separate locations have a relative instability reaching 7.5×10^{-14} at 1 s and 1.0×10^{-16} with 10 000-s averaging time, which is capable of transmitting the microwave atomic clocks, including state-of-the-art fountain clocks [37–40].

Compared with previous works, the major advantage of our work is the system setup using the all-optical link and the robust active noise cancellation. Considerable long-haul transmission instability can be achieved even without the help of electrical repeaters. These results not only affirm the viability of non-electrical-repeater long-haul O-TFT using OFCs, but also demonstrate the system's capability to effectively compensate for the severe fluctuations caused by thousand-kilometer-order long fiber links. This record-breaking implementation of O-TFT offers possibilities for ultra-long-haul O-TFT networks and paves the way for future large-scale time synchronization.

II. LONG-HAUL TRANSMISSION AND NOISE CANCELLATION METHODS

A. Experimental setup

The experimental setup of the long-haul O-TFT system is shown in Fig. 1. The Rb clock with instability of 2×10^{-12} at 1 s is used to provide the clock reference at the local

site. Two homemade OFCs at the local and remote sites respectively serve as the frequency transmission carriers. The bidirectional 3000-km fiber link is developed by 30 cascaded dense-wavelength division multiplexing (DWDM) units that have the same composition. Each unit consists of 100-km fiber, together with a dispersion compensation fiber (DCF) with fine-tuned length and a bi-EDFA, compensating for the link dispersion and attenuation, respectively. Similar to [16], in our setup the 30 distributed bidirectional optical amplifiers (EDFAs) are used to amplify the optical signals, effectively serving as optical repeaters in the frequency transfer system. The phase-noise compensation is designed based on the phase conjunction method [41] to ensure the phase consistency of the remote and reference signal. To evaluate the performance of the 3000-km frequency transfer system, we established an evaluation part connecting two sites' frequency signals by the phase-noise analyzer (Microchip, 53100A).

The OFCs with 1560-nm central wavelength and 10-nm 3-dB bandwidth generate optical pulse trains whose repetition rate is 100 MHz. The “figure-9 structure” of OFCs is used because it exhibits good stability and self-starting characteristics, which are desirable for our frequency transmission system in terms of low-noise and robustness requirements [42]. The comb's signal is filtered with international-telecommunication-union-standard DWDMs with 0.8-nm bandwidth so that we can obtain the C32 (1551.72 nm) and C34 (1550.12 nm) channels. In our scheme, the C32 channel is used for frequency transfer (forward direction) and the C34 channel is for phase discrimination and calculation (backward direction). A built-in EDFA in the OFC guarantees output optical power up to 100 mW, resulting in the power of each output being about 1 mW after filtering, which is sufficient for up to 100-km transmitting in the fiber link.

The OFC carries the signal by locking its repetition frequency to the reference (irrelevant to the combs' CEO

frequency, i.e., f_{CEO}), exploiting the locking control system (LCS) and cavity-length temperature feedback technique [36], which ensures the highly precise and long-term locking of OFCs' repetition rates to corresponding frequency references (for details see Appendix A). The frequency signal can be extracted by photodetecting the OFC signal, which also only keeps the envelope (equivalently, repetition frequency) information [43]. As a result, in our scheme only the repetition frequency needs to be manipulated, and the influence of f_{CEO} is discarded. Meanwhile, f_{CEO} plays a significant role in several other situations, and we leave it for future research.

The link-induced phase noise is compensated utilizing the phase conjunction method [41], which keeps the input signal phase conjugate of the round-trip signal phase. We write the phase time of the signals at each node of the system to clearly describe the compensation process. Supposing the clock's reference phase time $\tau_{\text{ref}}(t)$ and the direct digital frequency synthesizer (DDS) set phase time $\tau_{\text{DDS}}(t)$ (to be determined to compensate for the link phase noise), the link input and remote signal phase time after passing through the link are denoted as

$$\tau_{\text{in}}(t) = \tau_{\text{ref}}(t) + \tau_{\text{DDS}}(t), \quad (1)$$

$$\tau_r(t) = \tau_{\text{ref}}(t) + \tau_{\text{DDS}}(t) + \tau_f(t), \quad (2)$$

where $\tau_f(t)$ indicates the time-dependent phase-time fluctuation induced by the fiber link. The remote signal cannot be directly used by remote users due to the severe impact on its phase from the thousands-of-kilometers fiber link. To eliminate the fiber-induced phase noise, it is measured and compensated based on a basic principle that the forward and backward signals exert the same phase fluctuation $\tau_f(t)$, and the details are described below.

The fiber-induced noise can be obtained only by comparing the link input and output signal at the same site, so the second OFC locked to the signal with the phase time indicated by Eq. (2) is returned to the local end for phase discrimination. In other words, the round-trip signal, which carries double the link noise, is measured at the local site to estimate the practical phase variation at the remote site. To minimize the influence of back-scattering during round-trip transmission, the second OFC is phase-locked to the received pulse train at the remote site, whose spectrum is limited to the second filter range through different DWDM channels (C34 in our experiments), distinguishing from the forward transmission. Based on the aforementioned consideration, the phase-time fluctuation of the backward signal (i.e., the round-trip signal) is given by

$$\tau_{\text{rt}}(t) = \tau_{\text{ref}}(t) + \tau_{\text{DDS}}(t) + 2\tau_f(t), \quad (3)$$

which carries double the fiber-induced phase variation. The link drift $\tau_f(t)$ can be obtained by comparing Eq. (3) and Eq. (1) with our lock-in amplifier (LIA)-based digital method. Subsequently, the conjunction compensation is realized by setting the DDS,

$$\tau_{\text{DDS}}(t) = -\tau_f(t), \quad (4)$$

which ensures the link input signal phase time $\tau_{\text{in}}(t) = \tau_{\text{ref}}(t) - \tau_f(t)$ and the round-trip signal phase time $\tau_{\text{rt}}(t) = \tau_{\text{ref}}(t) + \tau_f(t)$ are conjugate, so that the remote signal is

phase time synchronized with the local reference signal $\tau_r(t) = \tau_{\text{ref}}(t)$ [41].

B. Compensation of link dispersion and attenuation

The 3000-km link in our experiment comprises 30 sets of 100-km standard commercial spooled fibers (G.652). The attenuation coefficient is 0.2 dB/km on average, and the second-order dispersion coefficient is 17 ps/(nm · km), resulting in the total attenuation exceeding 600 dB and the pulse broadening exceeding 40 ns. The transmitted signal would be unrecognizable without attenuation and dispersion compensation. To resolve these issues and ensure the similarity of each node in the follow-up analysis, we compensate the channel attenuation and dispersion after every 100 km of fiber.

As is shown in Fig. 1, in the fiber medium, the bandwidth-limited OFC carrying the frequency signal is sent to the fiber link after passing through the C32 channel (C34 for the opposite direction) of the DWDM module. The DWDMs not only effectively help utilize the channels, but also reduce the dispersion of the wide-spectrum OFC. To precisely compensate for the signal dispersion introduced in the corresponding link, a fine-tuned DCF is added after every 100 km of fiber. Each DCF has an attenuation of 7 dB and a dispersion of -1700 ps/nm on average, which exactly cancels with the 100-km-fiber-induced dispersion.

To compensate for the attenuation induced by each 100-km fiber and the corresponding DCF (about 27 dB in total), a bi-EDFA (two independent EDFAs with different filter bands in our work) is placed between two DWDMs to achieve round-trip and distributed amplification of the optical power. Since the multistage-amplification structure not only benefits the gain of a transmitted signal but also has an amplification effect on the amplified spontaneous emission noise of the previous stage, a self-developed low-noise EDFA with NF below 4.0 (the typical measured value is 3.8) is used to compensate for the channel attenuation, which shows great advantages, especially in long-haul cascaded transmission [29].

C. Compensation of link-induced noise

Through 30 cascaded 100-km link units, the ultimate pulse trains are detected by a commercial InGaAs PIN balanced photodetector with a bandwidth of 150 MHz (Thorlabs, PDB450C). A bandpass filter (BPF) with 100-MHz central frequency and 10-MHz bandwidth is used to filter the OFC repetition rate's first harmonic, for both generating frequency signal and the repetition-frequency locking of the OFC at the remote site. It is worth noting that the phase of the electrical signal generated by the optoelectric conversion of the photodetector is sensitive to its input power due to the APC process, which originates from the saturation of the photodetectors and is a combined effect of both the chip and the electronics [44–47]. We measured the impact of APC using our self-designed system and optimized it to an insignificant level.

1. Suppression of amplitude noise with active power stabilization

We visualized the APC process and quantitatively gave APC coefficient values of the specific photodetector used in

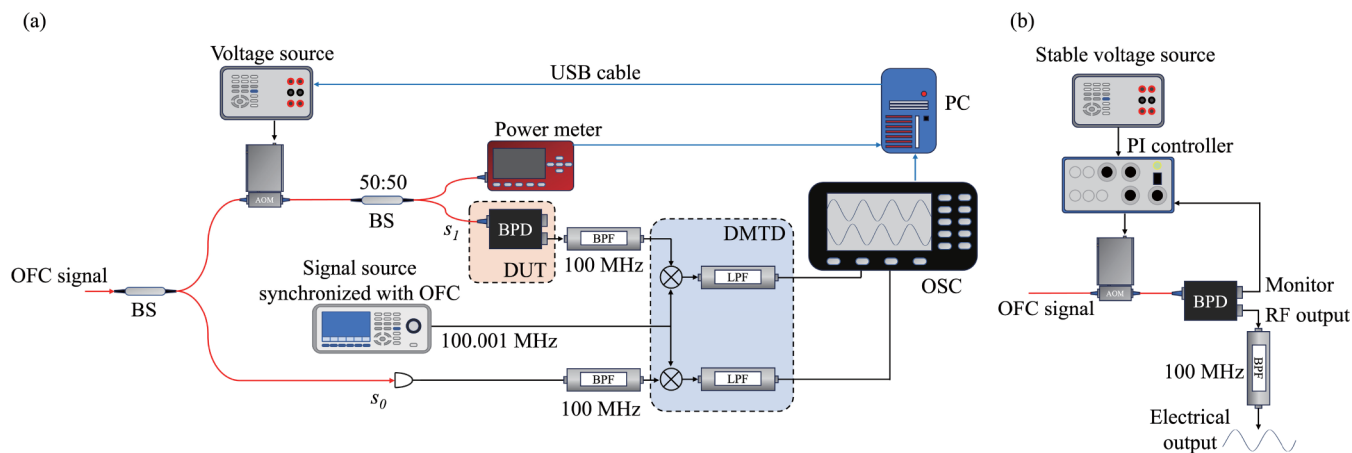


FIG. 2. Measurement and compensation scheme of amplitude-to-phase conversion (APC). (a) Experimental scheme measuring the APC coefficient. AOM, acoustic optical modulator; BS, beam splitter; BPD, balanced photodetector; DUT, device under test; BPF, bandpass filter; LPF, low-pass filter; DMTD, dual-mixer time difference; OSC, oscilloscope. (b) Active power stabilization system.

our experiment utilizing the setup in Fig. 2(a). An under-test comb signal is power-split into two branches, one serves as the phase reference (s_0) and the other one is fed into an acoustic optical modulator (AOM) that controls its output power with a programmable stable voltage source (Stanford Research Systems, model DC205). The AOM output is again split into another two branches, one is fed into a power meter (Thorlabs, PM100D) and the other one serves for phase detection after being photodetected and filtered with a 100-MHz BPF (s_1). An oscilloscope (OSC, RIGOL, MSO8204) connected by a PC is used to visualize and calculate the APC-induced phase variation. Since the OSC has an insufficient sampling rate (maximum 10 GHz), the dual-mixer time difference (DMTD) scheme is used to down-convert the under-test phase variation [48]. Specifically, a 100.001-MHz sinusoidal wave generated with an external signal source is mixed with the two under-test signals s_0 and s_1 , respectively, obtaining the low-frequency components with two low-pass filters,

$$\begin{aligned}
 s'_0(t) &= \text{LPF}\{\cos[(\omega + \Delta\omega)t] \times \cos[\omega(t - T_0)]\} \\
 &= \cos\left[\Delta\omega\left(t + \frac{\omega}{\Delta\omega}T_0\right)\right], \\
 s'_1(t) &= \text{LPF}\{\cos[(\omega + \Delta\omega)t] \times \cos[\omega(t - T_1)]\} \\
 &= \cos\left[\Delta\omega\left(t + \frac{\omega}{\Delta\omega}T_1\right)\right],
 \end{aligned} \quad (5)$$

where $\omega = 2\pi \times 100$ MHz and $\Delta\omega = 2\pi \times 1$ kHz. In this case the under-test phase time is amplified by $\alpha = \omega/\Delta\omega = 10^5$ times; consequently, the OSC has an equivalent maximum resolution of $1/(10 \text{ GHz} \times \alpha) = 1$ fs, which is sufficient for the subsequent experiment.

The APC measurement result is shown in Fig. 3(a). As the optical power increases from 0.02 to 1.85 mW (denoted by different colors), the phase of the detected DMTD signal gradually increases, approaching a maximum value indicative of the photodetector saturation process (provided the detector remains undamaged). The signal phase time has a total drift with the order of 1 ms, which means the original 100-MHz signal has drifted $1 \text{ ms}/\alpha = 10$ ns level due to the

optical power changes. We also note that as the optical power increases, the amplitude of the DMTD sinusoidal wave increases and gradually reaches a maximum value (about 0.2 V), which originates from the nonlinear output of the mixer devices [49].

To obtain the APC coefficient, which quantifies the phase-time change induced by RIN, we simultaneously record the relative phase time x and the current optical power P , and then calculate with [45]

$$C_{\text{APC}}(P) = \frac{\Delta x}{\Delta P/P} = \frac{\Delta x}{\Delta P} P \quad [\text{s}], \quad (6)$$

where the $\Delta x/\Delta P$ term is the slope of the black curve in the subfigure of Fig. 3(a). The calculated result is shown with the black solid curve in Fig. 3(b). As the power increases, the conversion coefficient initially increases and then decreases. At a power of 1.1 mW, the conversion coefficient reaches a peak value of 4.6 ns. In other words, when the signal exhibits a power fluctuation of 1%, it results in a phase-time variation of 46 ps, which significantly affects the system instability.

It is important to note that APC is a prevalent phenomenon across all photodetectors, albeit the APC curve may vary among different types and models of photodetectors. Typically, this necessitates calibration for subsequent experiments. In our approach, the phase fluctuation induced by APC in the frequency transfer system can be effectively mitigated through our proposed ‘‘calibration-power selection-active stabilization’’ process (which will be discussed in this section), regardless of the specific type of photodetectors utilized, as well as the APC response curves.

We measured the power variation of the link output signal (Fig. 4) and used it, along with the APC coefficient, to calculate the impact on the instability at 1 s, as shown by the red solid curve in Fig. 3(b). The APC has non-negligible effects on the system instability, which exceeds the order of 10^{-13} at 1 s.

To minimize the impact of APC on system instability, we propose a three-step solution: calibration, power selection, and active stabilization. Firstly, the APC curve of the

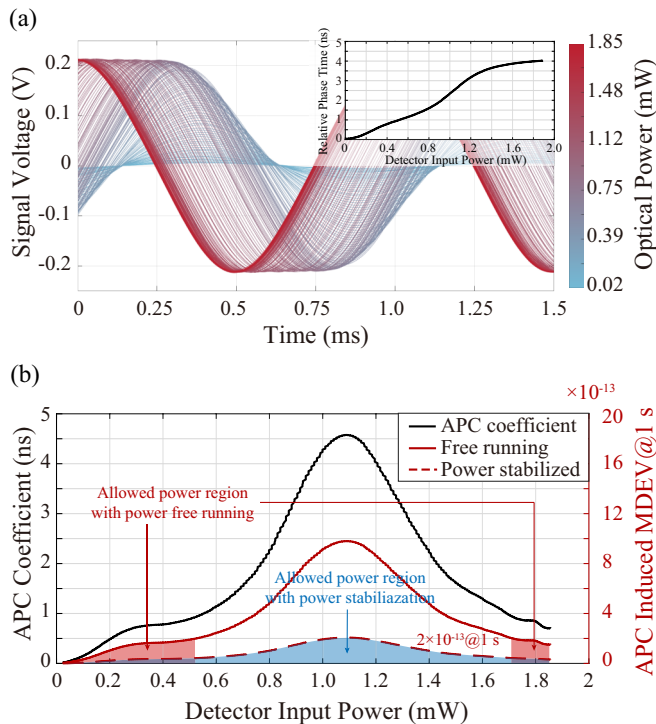


FIG. 3. Amplitude-to-phase conversion (APC) of the photodetector used in our experiment. (a) DMTD sinusoidal wave phase changes with optical power increases. (b) The black curve represents the measurement result of the APC coefficient. The solid-red and dashed-red curves represent the impact of APC on instability (modified Allan deviation at 1 s) before and after power stabilization, respectively. In order to keep the impact caused by APC below 2×10^{-13} at 1 s (as an example) without power stabilization, it is desired to control the average signal power to be less than 0.52 mW or greater than 1.71 mW (indicated by the red shaded area). For the case with active power stabilization, its impact on the instability is below 2×10^{-13} at 1 s at any average power value (blue shaded area).

photodetector is calibrated, as discussed above. Secondly, under a given RIN level, we manually select an average power with a smaller APC coefficient. For example, if the desired impact is to be below 2×10^{-13} at 1 s, the allowed power region is shown in Fig. 3(b) with the red shaded area. In our experiment we tested the power variations with average values of 1.1 and 0.5 mW by adjusting an optical attenuator, as shown in Fig. 4(a), with the corresponding instabilities depicted by the yellow and blue lines in Fig. 5. By selecting an appropriate average power level, we can optimize the instability caused by APC from 10^{-12} at 1-s level to 10^{-13} at the 1-s level. Thirdly, for further optimization the optical power is actively stabilized. We constructed a power stabilization system based on a PI controller to regulate the power of the signal entering the photodetector. As shown in Fig. 2(b), the under-test optical signal is sent into an AOM, whose output is detected with the photodetector, PDB450C. To extract the error signal that reflects the power variation, the monitor of PDB450C (DC-10 MHz components of the input signal) and a stable voltage supplied by DC205 serve as the two inputs of the PI controller (Newport, LB1005).

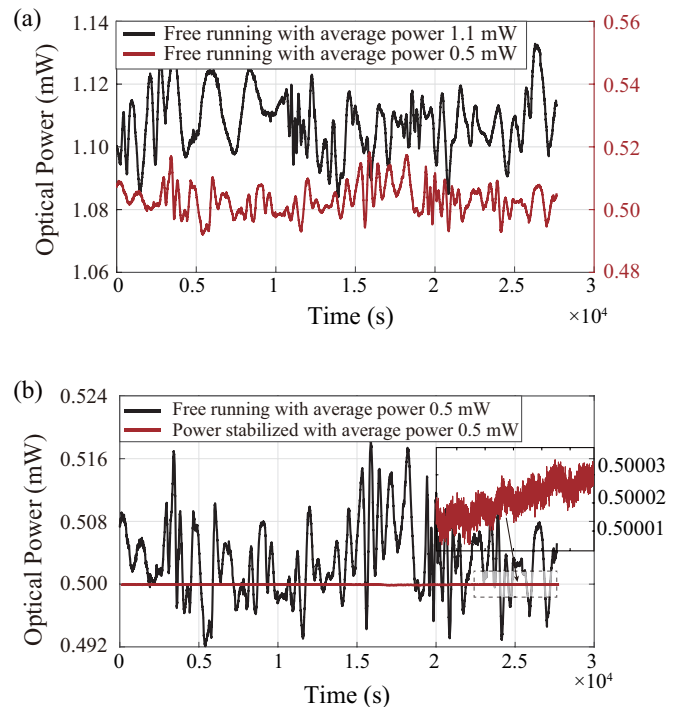


FIG. 4. Solutions to minimize the impact of APC on system instability. (a) Choosing an average power with a smaller APC coefficient. The figure shows the optical power variation with average values of 1.1 mW (at which the APC coefficient is 4.6 ns) and 0.5 mW (0.9 ns), respectively. (b) Active power stabilization. The figure shows the free-running optical power variation and actively stabilized optical power variation with an average value of 0.5 mW.

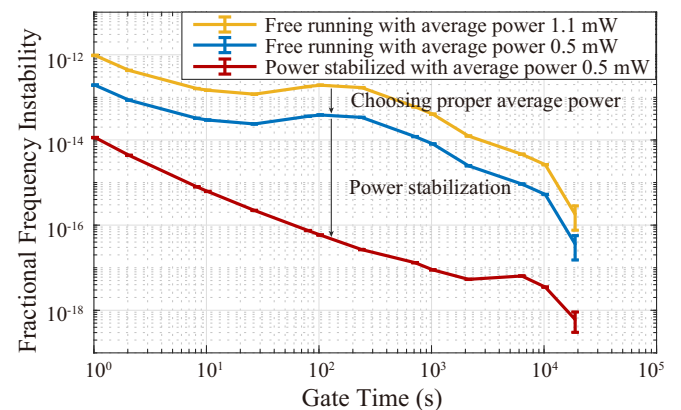


FIG. 5. Optical-power-variation-induced instability through amplitude-to-phase conversion (APC) and its optimization. The APC-induced frequency instabilities are calculated by $\sigma_{MDEV}\{\tau, x(t) = c_{APC}[\text{avg}(p(t))] \times p(t) / \text{avg}(p(t))\}$. The yellow curve is the free-running optical power with an average value of 1.1-mW induced frequency instability through APC. By choosing an average power of 0.5 mW that has a smaller APC coefficient, the free-running power induces lower instability as shown with the blue curve. The red curve shows the APC-induced instability with active power stabilization at 0.5 mW.

TABLE I. Correction-term value changes, e.g., when $\Delta\varphi$ increases from 0 and crosses $\pi/2$, the value of $\arctan(\Delta\varphi)$ skips to $-\pi/2$. Consequently, the correction term should plus π when the y has a positive value and x changes from positive to negative value (case 1).

Case	y value	x change	Correction change
1	+	$+\rightarrow-$	$+\pi$
2	+	$-\rightarrow+$	$-\pi$
3	-	$+\rightarrow-$	$-\pi$
4	-	$-\rightarrow+$	$+\pi$

The system, shown in Fig. 2(b), effectively stabilizes the power fluctuations and drifts, as demonstrated in Fig. 4(b) for a signal with an average power of 0.5 mW. The instability introduced by APC after power stabilization is depicted by the red curve in Fig. 5, where it is observed to reach a level of 1×10^{-14} at 1 s and 3×10^{-18} at 10 000 s, indicating a negligible impact on system instability. Additionally, we calculated the APC impact on the system instability at different average power levels using the stabilized power data, as shown by the red-dashed curve in Fig. 3(b). Overall, the impact remains below 2×10^{-13} at 1 s, indicating a minimal effect on system instability in comparison with the power-free-running case.

2. Infinite-dynamic-range digital phase discrimination

For long-haul transmission, the phase change caused by temperature fluctuation is always dramatic; see Fig. 10 in Appendix B. The large phase drift exceeding tens of signal periods for our 3000-km link results in a requirement for a larger dynamic range of measuring devices.

The round-trip phase variation is measured at the local site by the phase discrimination system. Distinguished from the mixer used in previous works, in this work we employ the LIA (Stanford Research Systems, SR844) with the resolution of 0.01° to discriminate the phase difference between local and round-trip signals.

The traditional mixer device, as shown in Fig. 6(a), has a nonlinear output voltage and one-to-many correspondence of the input phase difference, which brings difficulties when calculating the link-induced phase drift. LIA has a linear and one-to-one correspondence in a 2π period [Fig. 6(b)], while the cycle slip will still occur when the phase variation exceeds one period. To realize an unlimited dynamic range of phase discrimination, we utilize the x and y components output of the LIA to calculate the current phase value [Fig. 6(c)],

$$\Delta\varphi = \arctan\left(\frac{y}{x}\right) + \text{correction}, \quad (7)$$

where the correction term is determined by the cycles on Fig. 6(c). When $\Delta\varphi$ crosses the y axis, the correction term will plus or minus π to ensure the continuity of phase variation; specifically, see Table I.

Further, to validate the phase measurement nonlinearity (i.e., the deviation between the LIA-measured phase and the nominal value), we calibrated the LIA-measured phase data using a calibrated DDS, as depicted by the red curve in Fig. 7(a). As the DDS phase scans through one cycle (360°), the deviation between the measured phase time by LIA and

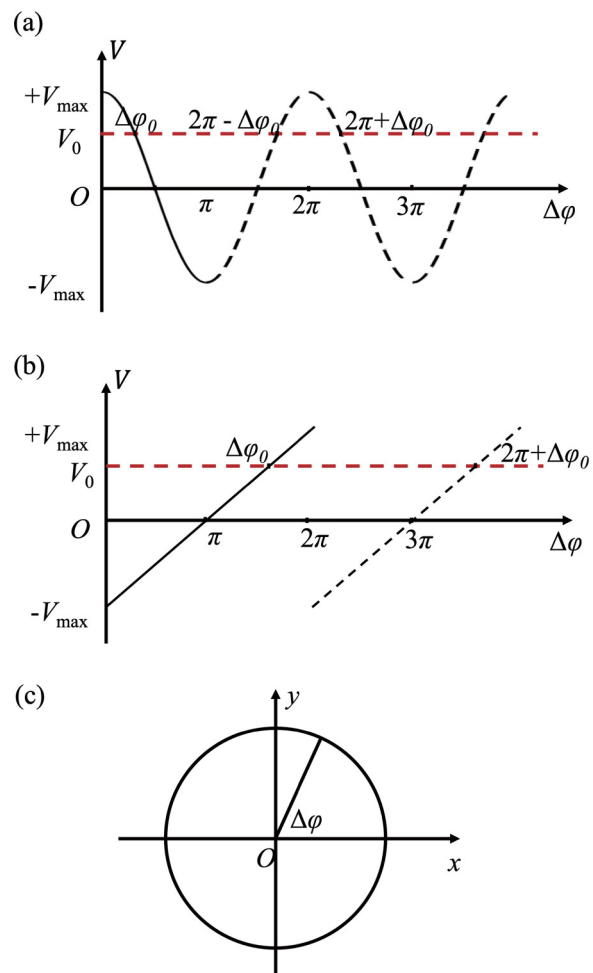


FIG. 6. Phase discrimination of a mixer device and a lock-in amplifier (LIA). (a) Mixer output voltage vs input signal phase difference; (b) LIA output voltage vs input signal phase difference; and (c) LIA x and y component output vs input signal phase difference.

the nominal value shows a sinusoidal correspondence with the peak value of 20 ps. Based on this result and incorporating the room-temperature variations (Fig. 10 in Appendix B), we simulated the impact of LIA nonlinearity on the system instability, which is constrained to 4×10^{-16} at 1000 s, as illustrated by the red curve in Fig. 7(b).

To compensate for this nonlinearity, ten sets of data at different nominal phase values are measured, averaged, and embedded into the Python acquisition program for calibration. During each data acquisition process, we apply real-time and efficient linear interpolation to correct the currently acquired phase data. The modified program yielded significantly improved results for the aforementioned experiment and simulation, as depicted by the black curves in Figs. 7(a) and 7(b). Up to now, our LIA-based digital phase discrimination system could accurately measure the phase difference of the round-trip phase difference, i.e.,

$$\Delta\tau_{\pi}(t) = \tau_{\pi}(t) - \tau_{\text{in}}(t) = 2\tau_{\text{f}}(t). \quad (8)$$

It is divided by 2 and serves as the phase to be compensated at the DDS.

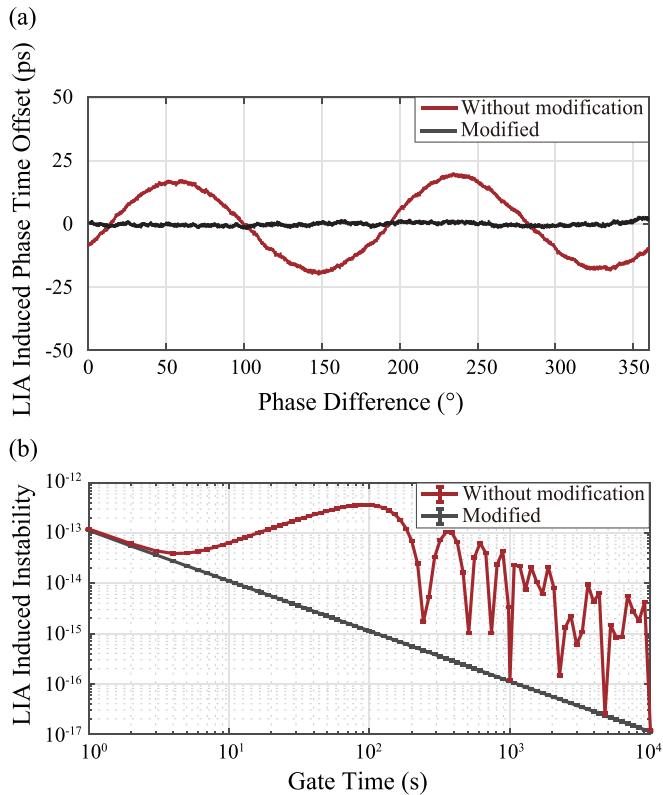


FIG. 7. Results of LIA nonlinearity. (a) LIA-nonlinearity-induced phase time offset in comparison with nominal value (red curve) and the modified result (black curve). (b) Simulated LIA-nonlinearity-induced system instability (red curve) and the modified result (black curve).

3. High-precision digital phase compensation

The system is compensated by the phase conjunction technique at the local site utilizing our homemade DDS. To fully compensate for the link-induced fast phase fluctuation, the homemade DDS has low additional instability at 5×10^{-14} at 1-s level and 16 digits (corresponds to 0.0055° resolution), which is below that of the LIA; for the long-term phase drift, the DDS has a complete 360° dynamic range and can cover and compensate any phase value. Figure 8 shows the homemade DDS is capable of continuously compensating a phase drift exceeding tens of periods of a 100-MHz signal without inducing any cycle slip. It significantly differs from the shorter transmission link (100 km or lower order) case, where the phase to be compensated is typically smaller than a signal cycle.

III. RESULTS OF THE LABORATORY 3000-KM FREQUENCY TRANSFER

With the help of the aforementioned techniques including low-NF EDFA, active power stabilization, LIA-based digital phase discrimination, and the homemade DDS, the 3000-km-fiber-induced instability is effectively suppressed to 7.5×10^{-14} at 1 s and 1.0×10^{-16} at 10 000 s. The experimental results are shown in Fig. 9. From the data of the phase-noise analyzer, we calculate the corresponding

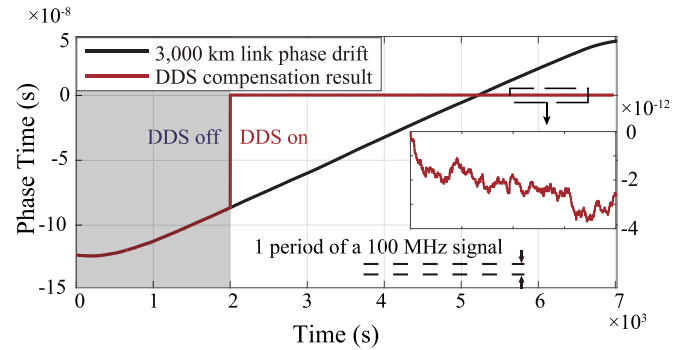


FIG. 8. The ability of DDS compensation. In the shaded area the system is free-running, while in the nonshaded area we show the free-running phase drift (black curve) and the DDS-compensated result (red curve) simultaneously.

fractional frequency instabilities of three different cases, i.e., the 3000-km link free-running, power-stabilized, and fully compensated (power and phase). Since the link is free-running before compensation, its frequency instability changes in a nonstationary manner, mainly caused by environmental changes. When the active power stabilization is on, it effectively suppresses the link instability to 9×10^{-13} at 1-s level, which leaves the uncompensated phase variation mainly determined by the common-mode temperature-induced phase changes. The high-precision digital phase discrimination and compensation method together enable stabilizing the link phase drift under large temperature turbulence.

In this work we note that the modified Allan deviation reaching 7.5×10^{-14} at 1 s is mainly limited by the LIA resolution at this stage. At 10 000 s of averaging time, the modified Allan deviation drops below 1.0×10^{-16} , over four orders of magnitude below the instability of the free-running link. The long-term instability could be further improved by installing temperature-control systems in EDFA elements.

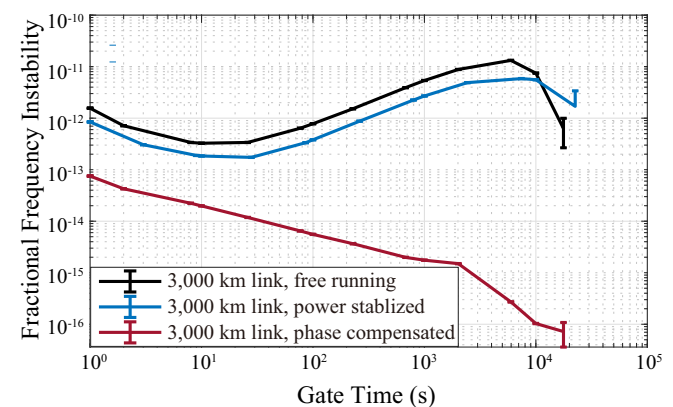


FIG. 9. Measurement result with and without compensation. The black curve indicates the instability of the 3000-km free-running link. The blue curve shows the link instability with average power selection and active power stabilization. The red curve shows the phase-noise-compensated result.

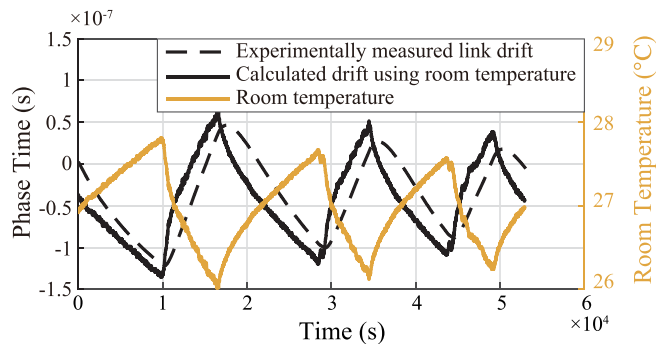


FIG. 10. Correspondence of the room temperature and the link phase drift. The black-dashed line is the experimentally acquired link phase drift, the yellow line is the temperature, and the black solid line is the calculated phase drift using Eq. (B1).

IV. CONCLUSION AND DISCUSSION

For ultra-long-distance frequency transfer, the tens-of-milliseconds fiber delay makes it impossible to fully suppress the link noise, confined by the delay-unsuppressed noise [50,51]. According to the simulation, it poses a limit at 1×10^{-14} at 1 s (see Appendix C), which our current compensated system has not yet approached. Consequently, for future optimization of our long-haul frequency transfer system, efforts should still focus on addressing issues related to the digital devices' noise and the non-common-mode noise, bringing the residual noise closer to the delay-unsuppressed noise limit.

We also note that the slope of the red curve in Fig. 9 changes from -1 to $-1/2$ at around 2000-s gate time originating from a quasiperiodical behavior whose period is about 2000 s. We attribute this phenomenon to temperature-related noise within the system, as evidenced by the similarity in the period to the temperature variations observed (around 2000 s, as depicted in Fig. 10, Appendix B). Such effects have been documented in various radio-frequency transfer studies and are likely rooted in the asymmetric components of the system, such as unequal propagation delays of the DWDM channels [52–54]. Further investigations into these temperature-related behaviors employing thermotanks would be of future interest to optimize the long-term performance of the system.

In summary, we show the realization of a frequency transfer system of over 3000 km of indoor fiber based on optical frequency combs. The transfer instability reaches 7.5×10^{-14} at 1 s and 1.0×10^{-16} at 10 000 s. The utilization of high-precision digital phase discrimination and compensation techniques and active power stabilization effectively suppresses the ultra-long-link-induced noise. The instability reported is enough to support the ultra-long-haul frequency transfer of state-of-the-art atomic microwave clocks. Our methods can provide better robustness in the face of large-range phase drift, e.g., under the condition of field tests. It thereby offers technical solutions to the atomic clock transmission scenarios aiming for longer transfer distances with larger channel attenuation and paves the way for construction of a larger-scale synchronization network.

ACKNOWLEDGMENT

This work was supported by the National Natural Science Foundation of China (Grants No. 62201012 and No. 61531003) and the China Postdoctoral Science Foundation (Grant No. 2020TQ0016).

APPENDIX A: FREQUENCY LOCKING OF THE OFCS

To achieve high-fidelity transfer of frequency, the repetition frequency of the OFC at the local site is phase-locked to the Rb clock by exploiting the locking control system, containing an electrical frequency multiplier, an optical-microwave phase detector [55], and a PI controller (Newport, LB1005S). The achieved residual frequency instability is superior to 1×10^{-14} at 1 s. Additionally, in order to achieve long-term phase-locking of the OFC to the reference oscillator, even when a large temperature variation occurs, an active cavity-length temperature feedback technique [36] is used to guarantee the stabilized phase-locking under severe temperature fluctuations over 5°C . In comparison, the source without using this technique supports the temperature change only for less than 0.5°C (corresponds to the 320-Hz repetition-frequency changes). This technology is realized via the fully human-free collaborative control of the thermoelectric cooler (TEC) and PZT voltage, and it greatly improves the robustness of the OFC-based system against changes in the external environment.

APPENDIX B: FIBER-INDUCED PHASE VARIATION

Here, to preliminarily evaluate the remotely-output signal, we show in Fig. 10 the measured phase drift after 3000-km transmission (black-dashed curve) and the laboratory's temperature variation (orange curve) at the same time. The phase drift could reach 150 ns in one day, and it covers 15 cycles of the 100-MHz signal (whose period is 10 ns). Further, we calculate the thermal effect relation that the time fluctuation obeys,

$$\begin{aligned} \Delta\tau_{\text{cal}}(t) &= \alpha L \Delta T(t) \\ &= 36.80 \text{ ps}/(\text{km } ^\circ\text{C}) \times L \times \Delta T(t), \end{aligned} \quad (\text{B1})$$

where $\alpha = 36.80 \text{ ps}/(\text{km } ^\circ\text{C})$ [56] is the calculated overall temperature coefficient, mainly attributed to the thermo-optic coefficient (refractive index variation with temperature) and the fiber's thermal expansion coefficient. Equation (B1) means that the 3000-km fiber link induces approximately 110.4-ns drift (i.e., about 11 periods of a 100-MHz signal) when the temperature changes 1°C . Following the above relation, the calculated data (black solid curve) fits the measured link phase drift well, and it reveals the origin of the system's phase drift comes from the temperature fluctuation. The violently varying phase drift poses a significant challenge to phase detection and compensation, highlighting the necessity of large dynamic range compensation with our proposed algorithm in the paper.

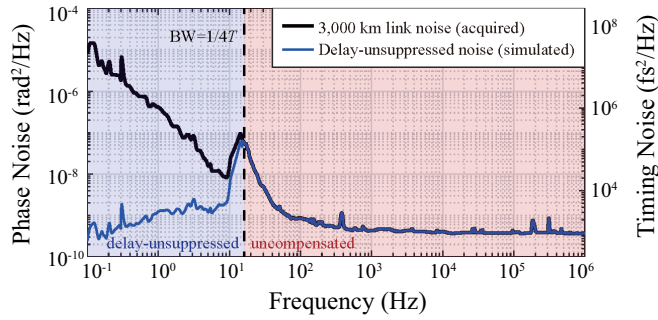


FIG. 11. Phase (and timing) noise spectral density of free-running 3000-km link [black curve, acquired by phase analyzer (Microchip, 53100A)] and the delay-unsuppressed noise [blue curve, simulated with blue curve and Eq. (C1)].

APPENDIX C: DELAY-UNSUPPRESSED NOISE OF OUR SYSTEM

The existence of the tens-of-milliseconds link delay indeed makes it impossible to fully suppress the fiber link noise and leaves the delay-unsuppressed noise to the evaluation result [50,51]. According to the derivation in the work [51], the delay-unsuppressed noise can be denoted as

$$S_{\text{unsuppressed}}(f) = \frac{1}{3}(2\pi fT)^2 S_{\text{fiber}}(f) \approx 3 \times 10^{-3} f^2 S_{\text{fiber}}(f), \quad (\text{C1})$$

where $S_{\text{fiber}}(f)$ is the free-running link phase noise, and T is the link delay, which is approximately 15 ms for our 3000-km link.

In Fig. 11 we show the phase (and timing) noise spectral density of the free-running 3000-km link (black curve) and the calculated delay-unsuppressed noise (blue curve) using Eq. (C1). In this result, it is clear that the phase noise in the low-frequency region (below $1/4T \approx 15$ Hz [57]) cannot

be fully canceled by the compensation system and is limited by the delay-unsuppressed noise. Furthermore, at higher frequencies the phase noise is totally uncompensated due to the compensation bandwidth limited by the link delay T [57]:

$$\text{BW}_{\text{compensation}} = \frac{1}{4T}. \quad (\text{C2})$$

Based on this result, we can analyze the influence on the system stability from the delay-unsuppressed noise by calculating the modified Allan deviation (MDEV) utilizing the transfer function [58]

$$\text{MDEV}(\tau) = \sqrt{\int_0^\infty \frac{f^2}{(2\pi\nu_0)^2} S_\phi^l(f) |H_M(jf)|^2 df}, \quad (\text{C3})$$

$$|H_M(jf)|^2 \approx 2 \frac{\sin^6(\pi\tau f)}{(\pi\tau f)^4}, \quad (\text{C4})$$

where τ is the gate time of the MDEV calculation, $\nu_0 = 100$ MHz is the central frequency of the signal, and $S_\phi^l(f)$ is the one-sided power spectral density (data in Fig. 11).

The estimated MDEV value at the 1-s gate time caused by delay-unsuppressed noise is

$$\text{MDEV}_{\text{unsuppressed}}(1 \text{ s}) = 1.0 \times 10^{-14}. \quad (\text{C5})$$

Compared with 7.5×10^{-14} at 1 s (the compensated result of our system), Eq. (C5) denotes that the unsuppressed noise brought by the 15-ms fiber delay is not the main contribution of our compensation result.

However, it is worth noting that the thousand-kilometer-level fiber link also brings other by-products. For instance, the compensation bandwidth is strictly limited by the tens-of-milliseconds-level fiber delay [Eq. (C2)], which leaves more uncompensated regions in the high-frequency domain. Simultaneously, the accumulation of higher frequency noise along the long fiber link, which cannot be mitigated by the compensation system due to the restricted compensation bandwidth, could exacerbate the system's performance.

- [1] F. Riehle, Towards a redefinition of the second based on optical atomic clocks, *C. R. Phys.* **16**, 506 (2015).
- [2] F. Riehle, P. Gill, F. Arias, and L. Robertsson, The CIPM list of recommended frequency standard values: Guidelines and procedures, *Metrologia* **55**, 188 (2018).
- [3] W. F. McGrew *et al.*, Towards the optical second: Verifying optical clocks at the SI limit, *Optica* **6**, 448 (2019).
- [4] J. Neil, L. Cosart, and G. Zampetti, Precise timing for vehicle navigation in the smart city: An overview, *IEEE Commun. Mag.* **58**, 54 (2020).
- [5] B. Jadiuszliwer and J. Camparo, Past, present and future of atomic clocks for GNSS, *GPS Solutions* **25**, 27 (2021).
- [6] E. D. Caldwell, L. C. Sinclair, N. R. Newbury, and J.-D. Deschênes, The time-programmable frequency comb and its use in quantum-limited ranging, *Nature (London)* **610**, 667 (2022).
- [7] I. Coddington, W. C. Swann, L. Nenadovic, and N. R. Newbury, Rapid and precise absolute distance measurements at long range, *Nat. Photon.* **3**, 351 (2009).
- [8] C. Lisdat *et al.*, A clock network for geodesy and fundamental science, *Nat. Commun.* **7**, 12443 (2016).
- [9] H. S. Margolis, Moving metrology, *Nat. Photon.* **1**, 258 (2007).
- [10] A. D. Ludlow, T. Zelevinsky, G. Campbell, S. Blatt, M. Boyd, M. H. de Miranda, M. Martin, J. Thomsen, S. M. Foreman, and J. Ye, Sr lattice clock at 1×10^{-16} fractional uncertainty by remote optical evaluation with a Ca clock, *Science* **319**, 1805 (2008).
- [11] R. M. Godun, P. B. R. Nisbet-Jones, J. M. Jones, S. A. King, L. A. M. Johnson, H. S. Margolis, K. Szymaniec, S. N. Lea, K. Bongs, and P. Gill, Frequency ratio of two optical clock transitions in $^{171}\text{Yb}^+$ and constraints on the time variation of fundamental constants, *Phys. Rev. Lett.* **113**, 210801 (2014).
- [12] N. Huntemann, B. Lipphardt, C. Tamm, V. Gerginov, S. Weyers, and E. Peik, Improved limit on a temporal variation of m_p/m_e from comparisons of Yb^+ and Cs atomic clocks, *Phys. Rev. Lett.* **113**, 210802 (2014).
- [13] A. Derevianko and M. Pospelov, Hunting for topological dark matter with atomic clocks, *Nat. Phys.* **10**, 933 (2014).
- [14] Y. V. Stadnik and V. V. Flambaum, Searching for dark matter and variation of fundamental constants with laser and maser interferometry, *Phys. Rev. Lett.* **114**, 161301 (2015).

- [15] K. Predehl *et al.*, A 920-kilometer optical fiber link for frequency metrology at the 19th decimal place, *Science* **336**, 441 (2012).
- [16] S. Droste, F. Ozimek, T. Udem, K. Predehl, T. Hänsch, H. Schnatz, G. Grosche, and R. Holzwarth, Optical-frequency transfer over a single-span 1840 km fiber link, *Phys. Rev. Lett.* **111**, 110801 (2013).
- [17] D. Hou, P. Li, C. Liu, J. Zhao, and Z. Zhang, Long-term stable frequency transfer over an urban fiber link using microwave phase stabilization, *Opt. Express* **19**, 506 (2011).
- [18] S. M. Foreman, K. W. Holman, D. D. Hudson, D. J. Jones, and J. Ye, Remote transfer of ultrastable frequency references via fiber networks, *Rev. Sci. Instrum.* **78**, 021101 (2007).
- [19] J. Ye, J. L. Peng, R. J. Jones, K. W. Holman, and L. S. Ma, Delivery of high-stability optical and microwave frequency standards over an optical fiber network, *J. Opt. Soc. Am. B* **20**, 1459 (2003).
- [20] K. W. Holman, D. J. Jones, D. D. Hudson, and J. Ye, Precise frequency transfer through a fiber network by use of 1.5- μm mode-locked sources, *Opt. Lett.* **29**, 1554 (2004).
- [21] S. Zhang and J. Zhao, Frequency comb-based multiple-access ultrastable frequency dissemination with 7×10^{-17} instability, *Opt. Lett.* **40**, 37 (2015).
- [22] H. J. Kang, J. Yang, B. J. Chun, H. Jang, B. S. Kim, Y.-J. Kim, and S.-W. Kim, Free-space transfer of comb-rooted optical frequencies over an 18 km open-air link, *Nat. Commun.* **10**, 4438 (2019).
- [23] Q. Shen, J.-Y. Guan, T. Zeng, Q.-M. Lu, L. Huang, Y. Cao, J.-P. Chen, T.-Q. Tao, J.-C. Wu, and L. Hou, Experimental simulation of time and frequency transfer via an optical satellite-ground link at 10^{-18} instability, *Optica* **8**, 471 (2021).
- [24] Q. Shen, J.-Y. Guan, J.-G. Ren, T. Zeng, L. Hou, M. Li, Y. Cao, J.-J. Han, M.-Z. Lian, Y.-W. Chen, X.-X. Peng, S.-M. Wang, D.-Y. Zhu, X.-P. Shi, Z.-G. Wang, Y. Li, W.-Y. Liu, G.-S. Pan, Y. Wang, Z.-H. Li *et al.*, Free-space dissemination of time and frequency with 10^{-19} instability over 113 km, *Nature (London)* **610**, 661 (2022).
- [25] E. D. Caldwell, J.-D. Deschenes, J. Ellis, W. C. Swann, B. K. Stuhl, H. Bergeron, N. R. Newbury, and L. C. Sinclair, Quantum-limited optical time transfer for future geosynchronous links, *Nature (London)* **618**, 721 (2023).
- [26] L. C. Sinclair, H. Bergeron, W. C. Swann, E. Baumann, J.-D. Deschênes and N. R. Newbury, Comparing optical oscillators across the air to milliradians in phase and 10^{-17} in frequency, *Phys. Rev. Lett.* **120**, 050801 (2018).
- [27] D. R. Gozzard, L. A. Howard, B. P. Dix-Matthews, S. F. E. Karpathakis, C. T. Gravestock, and S. W. Schediwy, Ultrastable free-space laser links for a global network of optical atomic clocks, *Phys. Rev. Lett.* **128**, 020801 (2022).
- [28] Ł. Śliwczynski, P. Krehlik, M. Lipiński, K. Turza, and A. Binczewski, Frequency distribution in delay-stabilized optical DWDM network over the distance of 3000 km, in *Joint Conference of the IEEE International Frequency Control Symposium & the European Frequency and Time Forum* (IEEE, New York, 2015), pp. 280–283.
- [29] D. Wang, T. Jiang, C. Liu, S. Zhou, and S. Yu, Stable radio frequency dissemination via a 1007 km fiber link based on a high-performance phase lock loop, *Opt. Express* **26**, 24479 (2018).
- [30] X. Zhang, L. Hu, X. Deng, Q. Zang, J. Liu, D. Jiao, J. Gao, R. Dong, T. Liu, and G. Wu, All-passive cascaded optical frequency transfer, *IEEE Photon. Technol. Lett.* **34**, 413 (2022).
- [31] H. Quan, W. Xue, W. Zhao, Y. Xing, H. Jiang, W. Guo, and S. Zhang, Microwave frequency dissemination over a 212 km cascaded urban fiber link with stability at the 10^{-18} level, *Photon.* **9**, 399 (2022).
- [32] W. Xue, W. Zhao, H. Quan, Y. Xing, and S. Zhang, Cascaded microwave frequency transfer over 300-km fiber link with instability at the 10^{-18} level, *Remote Sensing* **13**, 2182 (2021).
- [33] D. Yu, Z. Chen, X. Yang, Y. Xu, Z. Jin, P. Ma, Y. Zhang, S. Yu, B. Luo, and H. Guo, Time interval measurement with linear optical sampling at the femtosecond level, *Photon. Res.* **11**, 2222 (2023).
- [34] J.-D. Deschênes, L. C. Sinclair, F. R. Giorgetta, W. C. Swann, E. Baumann, H. Bergeron, M. Cermak, I. Coddington, and N. R. Newbury, Synchronization of distant optical clocks at the femtosecond level, *Phys. Rev. X* **6**, 021016 (2016).
- [35] I. Coddington, W. C. Swann, and N. R. Newbury, Coherent dual-comb spectroscopy at high signal-to-noise ratio, *Phys. Rev. A* **82**, 043817 (2010).
- [36] Z. Jin, Z. Chen, K. Wu, D. Yu, G. Wu, S. Yu, B. Luo, and H. Guo, Node-downloadable frequency transfer system based on a mode-locked laser with over 100 km of fiber, *Opt. Express* **31**, 39681 (2023).
- [37] T. N. Bandi, A comprehensive overview of atomic clocks and their applications, *BEMS Rep.* **9**, 01 (2023).
- [38] R. Wynands and S. Weyers, Atomic fountain clocks, *Metrologia* **42**, S64 (2005).
- [39] T. P. Heavner, E. A. Donley, F. Levi, G. Costanzo, T. E. Parker, J. H. Shirley, N. Ashby, S. Barlow, and S. Jefferts, First accuracy evaluation of NIST-F2, *Metrologia* **51**, 174 (2014).
- [40] S. Weyers, V. Gerginov, M. Kazda, J. Rahm, B. Lipphardt, G. Dobrev, and K. Gibble, Advances in the accuracy, stability, and reliability of the PTB primary fountain clocks, *Metrologia* **55**, 789 (2018).
- [41] G. F. Lutes, Optical fibers for the distribution of frequency and timing references, in *Proceedings of the 12th Annual Precise Time and Time Interval Systems and Applications Meeting, Greenbelt, Maryland* (Goddard Space Flight Center, Greenbelt, Maryland, 1980), pp. 663–680.
- [42] W. Hänsel, H. Hoogland, M. Giunta, S. Schmid, T. Steinmetz, R. Doubek, P. Mayer, S. Dobner, C. Cleff, M. Fischer, and R. Holzwarth, All polarization-maintaining fiber laser architecture for robust femtosecond pulse generation, *Appl. Phys. B* **123**, 41 (2017).
- [43] N. Haverkamp, H. Hundertmark, C. Fallnich, and H. R. Telle, Frequency stabilization of mode-locked erbium fiber lasers using pump power control, *Appl. Phys. B* **78**, 321 (2004).
- [44] E. N. Ivanov, S. A. Diddams, and L. Hollberg, Study of the excess noise associated with demodulation of ultra-short infrared pulses, *IEEE Trans. Ultrason. Ferroelectr. Freq. Control* **52**, 1068 (2005).
- [45] W. Zhang, T. Li, M. Lours, S. Seidelin, G. Santarelli, and Y. L. Coq, Amplitude to phase conversion of InGaAs pin photo-diodes for femtosecond lasers microwave signal generation, *Appl. Phys. B* **106**, 301 (2012).
- [46] R. Bouchand, D. Nicolodi, X. Xie, C. Alexandre, and Y. Le Coq, Accurate control of optoelectronic amplitude to phase

- noise conversion in photodetection of ultra-fast optical pulses, *Opt. Express* **25**, 12268 (2017).
- [47] M. Currie and I. Vurgaftman, Microwave phase retardation in saturated InGaAs photodetectors, *IEEE Photon. Technol. Lett.* **18**, 1433 (2006).
- [48] D. W. Allan and H. Daams, Picosecond time difference measurement system, in *Proceedings of the 29th Annual Symposium on Frequency Control, Atlantic City, NJ* (IEEE, Piscataway, NJ, 1975), pp. 404–411.
- [49] Y. Zhang, D. Yu, Z. Chen, T. Wu, and H. Guo, Parametric optimization of the practical mixer device in the optical comb frequency transfer system, in *Joint Conference of the European Frequency and Time Forum and IEEE International Frequency Control Symposium (EFTF/IFCS), Gainesville, FL* (IEEE, New York, 2021), pp. 1–3.
- [50] N. R. Newbury, P. A. Williams, and W. C. Swann, Coherent transfer of an optical carrier over 251 km, *Opt. Lett.* **32**, 3056 (2007).
- [51] P. A. Williams, W. C. Swann, and N. R. Newbury, High-stability transfer of an optical frequency over long fiber-optic links, *J. Opt. Soc. Am. B* **25**, 1284 (2008).
- [52] H. Li, G. Wu, J. Zhang, J. Shen, and J. Chen, Multi-access fiber-optic radio frequency transfer with passive phase noise compensation, *Opt. Lett.* **41**, 5672 (2016).
- [53] K. Turza, P. Krehlik, and L. Sliwczynski, Long haul time and frequency distribution in different DWDM systems, *IEEE Trans. Ultrason. Ferroelect. Freq. Control* **65**, 1287 (2018).
- [54] R. Huang, G. Wu, H. Li, and J. Chen, Fiber-optic radio frequency transfer based on passive phase noise compensation with frequency dividing and filtering, *Opt. Lett.* **41**, 626 (2016).
- [55] K. Jung and J. Kim, Subfemtosecond synchronization of microwave oscillators with mode-locked Er-fiber lasers, *Opt. Lett.* **37**, 2958 (2012).
- [56] Ł. Śliwczyński, P. Krehlik, and M. Lipiński, Optical fibers in time and frequency transfer, *Meas. Sci. Technol.* **21**, 075302 (2010).
- [57] W. Xue, H. Quan, W. Zhao, and S. Zhang, Microwave frequency transfer over a 500-km cascaded fiber link using tracking filter, *Opt. Laser Technol.* **163**, 109327 (2023).
- [58] E. Rubiola, *Phase Noise and Frequency Stability in Oscillators* (Cambridge University Press, Cambridge, UK, 2009).